Physics Letters A 444 (2022) 128237

Contents lists available at ScienceDirect

Physics Letters A

www.elsevier.com/locate/pla

# Transport barriers for two modes drift wave map

L.F. Bernardi de Souza [a], R. Egydio de Carvalho [a,*], I.L. Caldas [b]

[a] Universidade Estadual Paulista–UNESP, Instituto de Geociências e Ciências Exatas–IGCE, Departamento de Estatística, Matemática Aplicada e Ciências da Computação, 13506-900 Rio Claro-SP, Brazil
[b] Universidade de São Paulo–USP, Instituto de Física–IF, 05508-900 São Paulo-SP, Brazil

ARTICLE INFO

*Article history:*
Received 4 March 2022
Received in revised form 2 May 2022
Accepted 24 May 2022
Available online 30 May 2022
Communicated by A. Das

*Keywords:*
Drift waves
Two modes
Transport barrier
Shearless curve
Stickiness

ABSTRACT

Shearless barrier improves the plasma confinement and can be created by the application of a bias. Previously, they were identified with a 2D map of charged particle motion in one drift mode. Now, we add a second drift mode and derive a 3D map. By fixing the parameters related to the first mode and varying the second mode amplitude, we show that the existence of the barriers depends on the second mode amplitude. Winding number and recurrence times have been used to study the particle transport and the existence of the shearless. We also observe that even after the shearless destruction, the stickiness in its neighborhood continues to have a transport blocking effect to some extent. So, to evaluate the effectiveness of the barriers, we compute the ratio of initial conditions that crossed the barriers and by using the space parameter we highlighted the sensitivity of transport barriers to perturbations.



## 1. Introduction

Turbulence driven particle transport in magnetically confined plasmas is a recurrent and well-known transport phenomenon [1,2]. This commonly observed particle transport should be reduced to improve plasma confinement. Over the years, several control mechanisms have been implemented to reduce the particle transport, one of which is to change the radial contribution of the electric field through the application of an external electric potential [3].

Considering drift waves as a turbulence mechanism in tokamaks, a model was proposed in order to describe the particle transport as a consequence of chaotic motion and to explain its dependence on the radial electric field [4–6]. For nonmonotonic equilibrium electric field, the model allows a Hamiltonian approximation that leads to a nontwist nonlinear map with two coupled equations [4]. This map describes changes in the topology of regular structures in the phase space with the onset of shearless barriers [7], typical of nontwist maps [8–11], that limit the particle transport.

To investigate the plasma turbulence and the associated particle transport control, experiments have been performed in a new device, the Texas Helimak, specially designed to have discharges with different radial electric field equilibria. A recent work [12] used one-mode approximation for the drift wave model and for the study of the shearless barrier in the magnetically confined plasmas in nonmonotonic Texas Helimak equilibria. In the current work we added a second mode to the same model. One motivation to introduce this second mode is to improve the existing drift wave model and try to mimic the turbulent dynamics of the plasma.

For the modified model, we derive a map with three interdependent coordinates. By fixing the amplitude of the first mode and varying the amplitude of the second one, we investigate the existence of the shearless barriers, and we compute the critical parameter values for their destruction.

We also observe that even after the shearless barrier destruction, the stickiness in its neighborhood continues to have a transport blocking effect to some extent. So, in order to evaluate the effectiveness of the barriers, we compute the ratio of initial conditions that crossed the barriers in terms of the parameters related to the modes and by using the space parameter we highlighted the sensitivity of transport barriers to perturbations.

In Section 2 we introduce the model and derive the new map. The transport barrier effectiveness is analyzed in Section 3, and the conclusions are given in Section 4.

## 2. The model

Investigations about the turbulence and transport in tokamak present difficulties, due to its geometry. Considering this issue, the Texas Helimak (TH hereafter) was developed, which is a device designed with a simpler geometry than tokamaks to perform mag-

* Corresponding author.
*E-mail addresses:* luis.souza@unesp.br (L.F. Bernardi de Souza), ricardo.egydio@unesp.br (R. Egydio de Carvalho), ibere@if.usp.br (I.L. Caldas).

https://doi.org/10.1016/j.physleta.2022.128237
0375-9601/

netized experiments that reproduce selected plasma characteristics at the edge of the tokamaks. The TH consists of a circular vessel and helical magnetic field lines. The magnetic field has a toroidal and a vertical component expressed by,

$$\vec{B} = B_\varphi \hat{e}_\varphi + B_z \hat{e}_z \tag{1}$$

The helicity of the field lines is the inverse of the safety factor given by [13],

$$q = \frac{H B_\varphi}{r B_z} \tag{2}$$

in which $H$ is the height of the TH camera. The plasma equilibrium has vertical and radial electric field components.

Due to the circular component of the magnetic field, a vertical electric field appears and, consequently an electric drift velocity. This velocity has a radial component that pushes the plasma against the wall of the machine [12].

The fluctuations in TH are present in the whole plasma and they depend on the radial electric field and density profiles [14]. In the analyzed experiments the radial electric field can be modified by a bias, an external electric potential applied in a set of plates [12,13]. Thus, turbulence-driven particle transport can be modified, and its properties investigated. This turbulence, as the one observed in the scrape-off layer of tokamaks, is essentially electrostatic with a different spectrum from the magnetic fluctuations [13–16]. In TH, the magnetic fluctuations are even negligible [13].

For a better approximation of the model, experimental data from [17–19] were used to estimate the map's control parameters and for numerical simulations. We limited the study for two positive bias values (4 and 8 Volts).

### 2.1. Two-modes drift wave map

The drift wave model [4] assumes that the motion of the particles is dictated by the drift $\vec{E} \times \vec{B}$ so, the particle motion equation or the guiding center equation is given by,

$$\frac{d\vec{x}}{dt} = \upsilon_{||} \frac{\vec{B}}{B} + \frac{\vec{E} \times \vec{B}}{B^2} \tag{3}$$

in which $\vec{x}$ is the position vector of the particles, $\upsilon_{||}$ is the velocity modulus of the particles parallel to the circular component of the magnetic field $\vec{B}$. In the TH, the electric field is composed by two terms, an equilibrium radial field $E_0$ and a perturbative component $\vec{\tilde{E}}$ so that,

$$\vec{E} = E_0 \hat{e}_r + \vec{\tilde{E}} \tag{4}$$

and they are derived from a perturbative electrostatic potential,

$$\vec{\tilde{E}} = -\vec{\nabla}\tilde{\phi} \tag{5}$$

The model includes the drift wave effect as a turbulence mechanism i.e., the perturbative term is written in cylindrical coordinates $(r, \varphi, z)$ as the expansion,

$$\tilde{\phi}(\vec{x}, t) = \sum_{l,m,n} \phi_{l,m,n} cos(m\varphi - l_z z - n\omega_0 t) \tag{6}$$

in which $\phi_{l,m,n}$ is the amplitude of the waves, $\omega_0$ is the lowest angular frequency in the drift wave spectrum and $l_z = 2\pi\ l/H$ $(l = 1, 2, 3...N)$. Using the following identities,

$$\sum_{n=-\infty}^{\infty} cos(n\omega_0 t) = 2\pi \sum_{n=-\infty}^{\infty} \delta(\omega_0 t - 2\pi n) \tag{7}$$

$$\sum_{n=-\infty}^{\infty} sin(n\omega_0 t) = 0 \tag{8}$$

the electrostatic potential (6) can be written as,

$$\tilde{\phi} = 2\pi \sum_{l,m,n} \phi_{l,m,n} cos\,(m\varphi - l_z z)\, \delta(\omega_0 t - 2\pi n) \tag{9}$$

In TH, the magnitude of the vertical component of the magnetic field $(B_z)$ is at most 10% of the magnitude of the circular component $B_\varphi$ [5], so the approximation can be made, $B \approx B_\varphi \gg B_z$, therefore the decomposition of equation (3) in each coordinate results in,

$$\frac{dr}{dt} = \frac{1}{B} \frac{\partial \tilde{\phi}}{\partial z} \tag{10}$$

$$r \frac{d\varphi}{dt} = \upsilon_{||} \tag{11}$$

$$\frac{dz}{dt} = \upsilon_{||} \frac{B_z}{B} + \frac{E_0}{B} - \frac{1}{B} \frac{\partial \tilde{\phi}}{\partial r} \tag{12}$$

The drift wave model is composed of infinite spatial modes which are denoted by m and l in equation (6). In our current approach we consider two spatial modes in the electrostatic potential of equation (6), which we call by (M, L) for the first mode and (M + 1, L) for the next consecutive mode. Thus, the infinite spatial modes model is adjusted to only two dominant spatial modes. The choice of the values of M and L was based in experiments with the TH and reported in [18]. In fact, we considered that the experimental power spectra have a broad frequency interval and a narrow wave number interval. This profile allows us to assume two modes with different wave numbers and the same frequencies. Therefore, the electrostatic potential (6) is approximated as,

$$\tilde{\phi} = 2\pi \left\{ \phi_{M,L} \cos[M\varphi - Lz] + \phi_{M+1,L} \cos[(M+1)\varphi - Lz)] \right\} \times \sum_n \delta(\omega_0 t - 2\pi n) \tag{6'}$$

It is now convenient to make the following variables change,

$$I = \frac{r^2 - R_{int}^2}{R_{ext}^2 - R_{int}^2} \tag{13}$$

$$\chi = M\varphi - Lz \tag{14}$$

where $R_{int}$ and $R_{ext}$ are internal and external radius of the TH, respectively. The coordinate $\chi$ is an angle and $I$ is the action variable. Therefore, from (13) and (14) on, the equations of motion are written in the action-angle coordinates. The perturbative term (9) consists of periodic pulses of period $T = 2\pi/\omega_0$, so that the integration of equations (13) and (14) is done between two consecutive pulses, however the coordinate $\chi$ has a term in $\varphi$, so it is also necessary to integrate equation (11) in the same interval as $I$ and $\chi$. Hence, the two-mode nonlinear drift wave map is given by,

$$I_{n+1} = I_n + \alpha_1 sin\chi_n + \alpha_2 sin(\chi_n + \varphi_n) \tag{15a}$$

$$\chi_{n+1} = \chi_n + \frac{\beta}{\sqrt{I_{n+1} + b^2}} \tag{15b}$$

$$\varphi_{n+1} = \varphi_n + \frac{\gamma}{\sqrt{I_{n+1} + b^2}} \tag{15c}$$

with $b^2 \equiv \frac{R_{int}^2}{R_{ext}^2 - R_{int}^2}$. The control parameters $\alpha_1$, $\alpha_2$, $\beta$ and $\gamma$ are defined as,

$$\alpha_1 \equiv \frac{4\pi L \phi_{M,L}}{\omega_0 q(I_n) a^2 B_z} \tag{16}$$

$$\alpha_2 \equiv \frac{4\pi L \phi_{M+1,L}}{\omega_0 q\,(I_n)\, a^2 B_z} \tag{17}$$

$$\beta \equiv \frac{2\pi}{\omega_0 a q\,(I_n)} \left[ \upsilon_{||}\,(Mq\,(I_n) - L) - \frac{LE_0}{B_z} \right] \tag{18}$$

$$\gamma \equiv \frac{2\pi\,\upsilon_{||}}{\omega_0 a} \tag{19}$$

$q$ is the safety factor which is kept constant as q = 2.89 according to [19]. $E_0$ is the equilibrium electric field and $a \equiv \sqrt{R_{ext}^2 - R_{int}^2}$.

Comparing this set of equations with one used in [12], we observe that the presence of the second mode results in an additional coupled equation for $\varphi_{n+1}$ and four control parameters. We assumed $q, \phi_{M,L}, \phi_{M+1,L}$ constants and $M = 2$ and $L = 3$. Although the new map has three coupled coordinates, the phase spaces will be displayed in action-angle coordinates (I, $\chi$).

The control parameters $\alpha_1$ and $\alpha_2$ are related to the amplitude of the waves, according to (16) and (17). The parameter $\beta$ is related to the equilibrium electric field $E_0(I)$ which we will assume with a quadratic radial profile. The choice for the radial approximation of the electric field profiles changes the properties of the map, leading to topological rearrangements in the phase space. More specifically, choosing a nonlinear radial profile for the electric field leads to the violation of the twist condition what can introduce at least one shearless curve in the phase space [9].

For null wave amplitudes, i.e., $\phi_{M,L}$ and $\phi_{M+1,L}$ equal to zero, implies that $\alpha_1$ and $\alpha_2$ are also nulls according to (16) and (17), therefore the map represents an integrable system and the orbits in the phase space will be represented by invariant curves, for any initial condition $I_0$. For non-null values of the wave amplitudes, the phase space presents regular structures and chaotic orbits. One method of evaluating the nature of the orbits in non-integrable systems is through the winding number. For a given initial condition $\chi_0$, the winding number is defined as,

$$\Omega = \lim_{n\to\infty} \frac{\chi_n - \chi_0}{n} \tag{20}$$

and $n$ is a great number of iterations.

If the winding number profile has an extreme (local maximum or minimum), the coordinates corresponding to the extreme identify a point over the shearless curve in the phase space. The shearless curve has the important characteristic of being quite robust under the effect of perturbations and for the plasma confinement problem, the destruction of the shearless curve indicates lack of particle confinement causing particle lost in the system [12].

In addition to the winding number profile, another numerical method to analyze the shearless curve, or any quasi-periodic orbits, is by the Slater's theorem [20], which says for a quasi-periodic orbit there are at most three different recurrence times, denoted by $\Gamma_1$, $\Gamma_2$ and $\Gamma_3 = \Gamma_1 + \Gamma_2$. Therefore, calculating the recurrence times it is possible to determine if the orbit is quasi-periodic or chaotic [21,22].

In the next sections, will be evaluated the influence of the second mode in the phase space, the critical parameters values of which the shearless curve is destroyed and the effectiveness of the transport barriers in terms of the map's control parameters.

### 2.2. Effect of the second mode

In [6], the bias influence was carried out by setting −10 V for the wave's amplitude, therefore, we keep this same amplitude for the first wave, i.e., $\phi_{M,L}$ also assumes −10 V. Next, we vary gradually the second wave amplitude ($\phi_{M+1,L}$). We choose only the bias 4 and 8 Volts because the shearless barrier is present for both cases when the amplitude of the first wave is set to −10 V [6]. The coordinates were normalized between 0 and 1. An escape condition

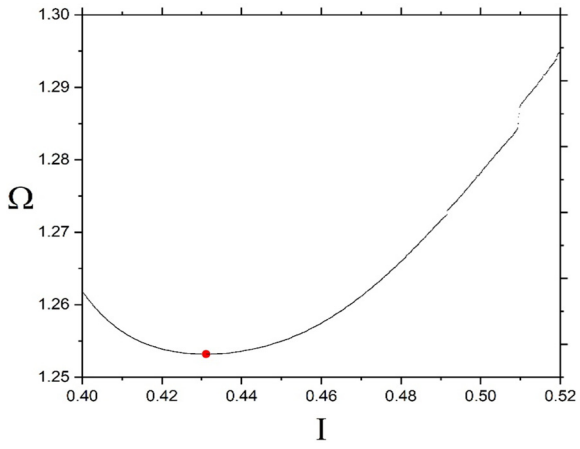


**Fig. 1.** The winding number profile for $\chi_0 = 0.5$ and several values of I, the red dot (I = 0.4308, $\Omega = 1.2532$) allows to choose an initial condition on the shearless curve for 4 Volts bias. (For interpretation of the colors in the figure(s), the reader is referred to the web version of this article.)

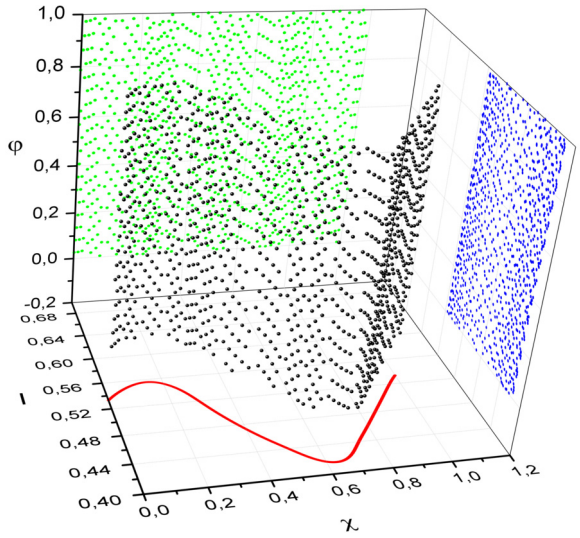


**Fig. 2.** Perspectives in the space (I, $\chi$, $\varphi$). In black the iterations of the initial condition; in red the shearless curve in the projected phase space (I, $\chi$); in blue the phase space (I, $\varphi$) and in green the configuration space ($\chi$, $\varphi$). The shearless curve appears only in the projection (I, $\chi$).

$\sqrt{I_{n+1}^2 + b^2}$ was also considered, this means that iterations of $I$ was interrupted when $I_{n+1}^2 < b^2$. For the winding number profiles, the initial condition was $\chi_0 = 0.5$ and $\varphi_0 = 0.5$ with $10^4$ iterations. For both bias values, as $\phi_{M,L} = -10$ V then $\alpha_1 = -0.09423$. Along the numerical calculation the values of $\phi_{M+1,L}$ were implicitly obtained by varying conveniently the values of $\alpha_2$.

The addition of a second mode introduced a new coordinate in relation to the one-mode map [4,12], therefore the dynamics is governed by a map with three coordinates (I, $\chi$, $\varphi$), but the most significant results occur when we analyze the dynamics in the plane ($\chi$, I). The main result that led us to this conclusion was that the shearless curve appeared only in the ($\chi$, I) plane. In Fig. 1 we present the winding number profile, with $\alpha_2 = 0$, for the case of 4 Volts bias and we can see a minimum point, what identifies a point belonging to the shearless curve.

In Fig. 2 we show iterations, in black color, of this identified point on the shearless curve in the 3d space (I, $\chi$, $\varphi$). We see that the shearless curve appears only when the dynamic is projected in the ($\chi$, I) plane, color red, while in the other projections, ($\varphi$, I), color blue, and ($\varphi$, $\chi$), color green, it does not appear. Hence, from

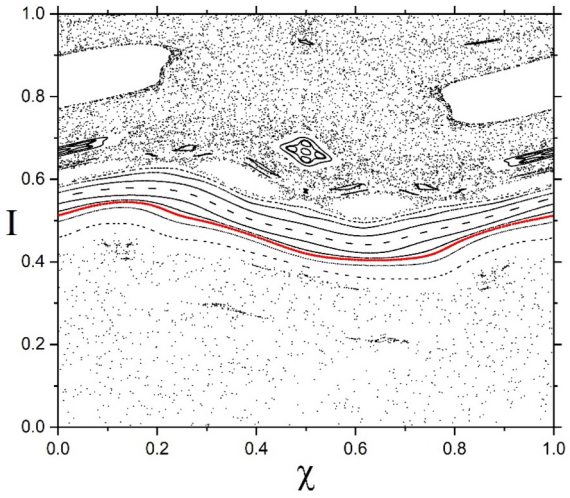


**Fig. 3.** The phase space $(I, \chi)$ with $\alpha_1 = -0.09423$ and $\alpha_2 = 0$, for 4 Volts bias. The shearless curve is in red.

now on the investigations of the influence of the second mode in the dynamics will only occur in the plane $(\chi, I)$. The same behavior was found for the 8 Volts bias case.

In Fig. 3 the phase space with $\alpha_2 = 0$ was obtained by iterating 100 times the map equations for 50 initial conditions. The obtained phase space shows invariant curves and resonance islands in the central region with the chaotic sea divided in two regions, highlighted in red is the shearless curve. The shearless curve was iterated with the initial condition identified by the minimum point in the winding number profile in Fig. 1. The barriers splitted the chaotic region, avoiding the internal trajectories to escape to the wall and improving the plasma confinement. Furthermore, the presence of the shearless curve for $\alpha_2 = 0$ is of great importance as we now have a reference for comparisons when the second mode enters in the dynamics.

We present in Fig. 4a the phase space $(\chi, I)$, for $\alpha_2 = -0.01633$ (the critical value for the shearless), using two colors, red and green, representing iterations of each 12 initial conditions above and below, respectively, where the shearless curve was previously located. We iterated each initial condition $10^4$ times, where we observe that the orbits are limited and separated by a high density of points at the place where was the shearless torus. This effect is called stickiness and this region continues blocking the transport

**Table 1**
Slater Recurrence Times (4 Volts bias) for the shearless curves with three different values of $\alpha_2$ and fixed $\alpha_1 = -0.09423$. When $\alpha_2 = -0.01633$ the shearless torus is destroyed. The initial conditions used on the shearless are $(I, \chi, \varphi) = (0.4308, 0.5, 0.5)$.

| $\alpha_2$ | $\Gamma_1$ | $\Gamma_2$ | $\Gamma_3$ |
|---|---|---|---|
| −0.01611 | 4 | 104 | 108 |
| −0.01622 | 4 | 104 | 108 |
| −0.01633 | 4 | 73 | 108 |

in the phase space for a high number of iterations. It can appear just after the destruction of the shearless curve [10,23]. Fig. 4b shows the orbits mixing with the value of $\alpha_2 = -0.05033$.

As the amplitude of the second wave is increased, the regular structures begin to be destroyed leading to a rising sea of chaos. In order to evaluate the effects of the perturbation on the shearless barrier, we computed the Poincaré recurrence times for the shearless curve using as initial condition the minimum of the winding number profile, Fig. 1. The Poincaré recurrence time theorem states that in dynamical systems an orbit will return to a state arbitrarily close to its initial state after a sufficiently long, but finite, time [20]. On other hand, an adapted version of Slater's theorem for dynamical systems states that a translation over irrational tori returns to an arbitrary interval in at most three different recurrence times, so that the largest of them is the sum of the smallest ones [21,22].

In Table 1 we present recurrence times numerically obtained for three values of $\alpha_2$. Since the Slater's recurrence time condition is violated for $\alpha_2 = -0.01633$, we know that the shearless barrier does not exist for this value. Moreover, we verify that this value of $\alpha_2$ is the critical value for the shearless barrier destruction, i.e., when $\alpha_2$ reaches $-0.01633$ the shearless torus is destroyed.

Similar results were obtained for the 8 V bias case. Without the presence of the second wave, the phase space in Fig. 5a) shows regular structures dividing and limiting the chaotic orbits into two separated regions and highlighted in red is the shearless curve. The shearless torus is easily identified as being the minimum of the winding number profile in Fig. 5b).

For the shearless torus with the second mode on, according to the recurrence times presented in Table 2, $\alpha_2 = -0.01082$ is the critical value since the recurrence times no longer obey the condition of Slater's theorem.

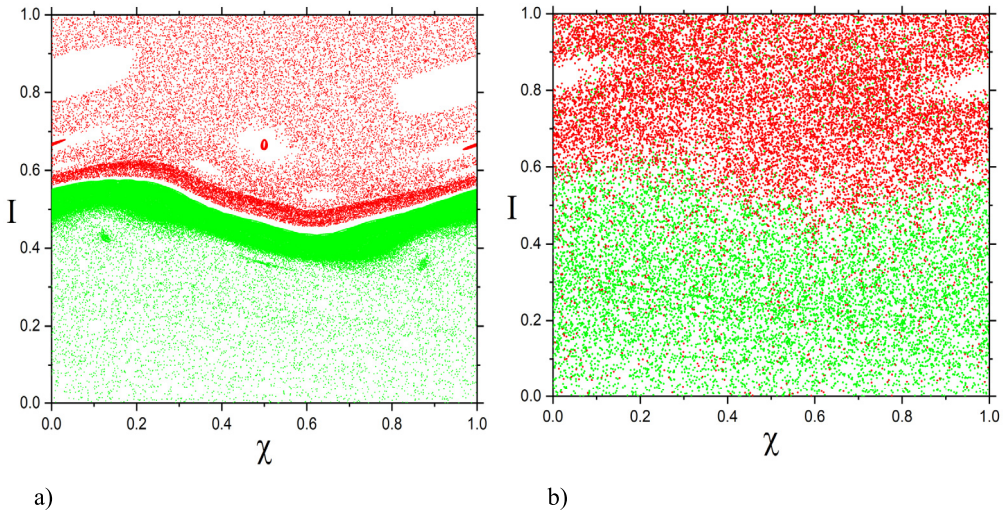


**Fig. 4.** Phase spaces for the 4 Volts bias case with $\alpha_1 = -0.09423$, $\varphi_0 = 0.5$, $\chi_0 \in [0, 1]$ and were given 12 initial conditions in the red region for $I_0 \in [0.7, 0.8]$ and 12 in the green region for $I_0 \in [0.2, 0.3]$. In a), $\alpha_2 = -0.01633$, we see the stickiness blocking the transport. In b), $\alpha_2 = -0.05033$, we see the orbits mixing.

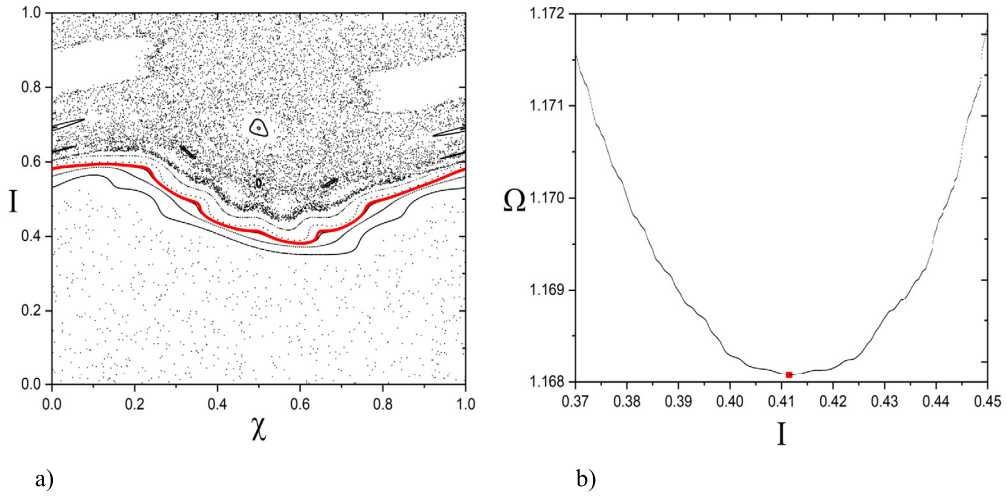


**Fig. 5.** In a) phase space with $\alpha_1 = -0.09423$ and $\alpha_2 = 0$ (8 Volts bias) showing the shearless curve highlighted in red. In (b) the winding number profile for the same parameters, the red dot (I = 0.4115, $\chi = 1.6810$) allows to choose an initial condition on the shearless curve.

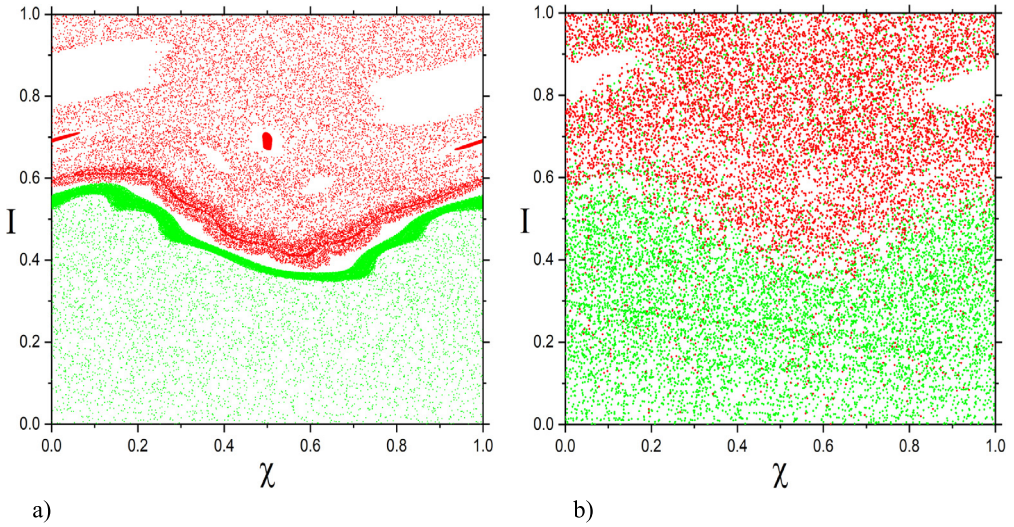


**Fig. 6.** Phase spaces for the 8 Volts bias case with $\alpha_1 = -0.09423$, $\varphi_0 = 0.5$, $\chi_0 \in [0, 1]$ and were given 12 initial conditions in the red region for $I_0 \in [0.7, 0.8]$ and 12 in the green region for $I_0 \in [0.2, 0.3]$. In a), $\alpha_2 = -0.01088$, we see the stickiness blocking the transport. In b), $\alpha_2 = -0.04082$, we see the orbits mixing.

**Table 2**
Slater Recurrence Times (8 Volts bias) for three different values of $\alpha_2$ with $\alpha_1 = -0.09423$. When $\alpha_2 = -0.01082$ the shearless torus is destroyed.

| $\alpha_2$ | $\Gamma_1$ | $\Gamma_2$ | $\Gamma_3$ |
|---|---|---|---|
| −0.01061 | 6 | 71 | 77 |
| −0.01071 | 6 | 71 | 77 |
| −0.01082 | 6 | 56 | 71 |

For the 8 Volts bias case, with the increase of the amplitude of the second wave, the regular structures are gradually substituted by chaotic orbits as we can see in Fig. 6a with $\alpha_2 = -0.01082$. Similarly to the 4 Volt bias case, the orbits of the red and green regions are still limited and do not mix in the phase space due to the high density of points where the invariant torus was located, evidencing the existence of a temporary transport barrier constituted by a region of stickiness. In Fig. 6a we iterated each initial condition $10^4$ times. Fig. 6b shows the orbits mixing with the value of $\alpha_2 = -0.04082$.

With the destruction of the shearless curve, and the other invariant curves, it is expected that the chaotic orbits would spread throughout the phase space, however transport blocking effects are still present. Fig. 4 and Fig. 6 show, for both bias values, that where the invariant curves were initially located there is a stickiness layer formed by a high density of points making it difficult for the chaotic orbits to access the entire phase space even after the invariant torus destruction.

## 3. Transport barrier effectiveness

Previously, the transport barrier study [12] was limited to compute the critical parameter values of the shearless curve destruction for one perturbing mode, but its robustness was not evaluated. Now we evaluate this robustness by considering the perturbation caused by a second mode, in terms of the control parameters $\alpha_1$ and $\alpha_2$, regardless of which kind of barrier is causing the blockage, the invariant curves, the shearless torus or the stickiness.

Fig. 7a and Fig. 7b show the space of parameters ($\alpha_2$, $\alpha_1$) depicted in a color scale, using the ranges $\alpha_1 \in [-0.15, 0]$ and $\alpha_2 \in [-0.2, 0]$. This choice was made after many numerical simulations. Each parameter interval was varied in steps of $10^{-3}$ and for each pair $\alpha_1$ and $\alpha_2$, 2500 initial conditions were given in the chaotic region. Next, the map was iterated $1 \times 10^6$ times for each initial condition and finally was collected the initial conditions ra-

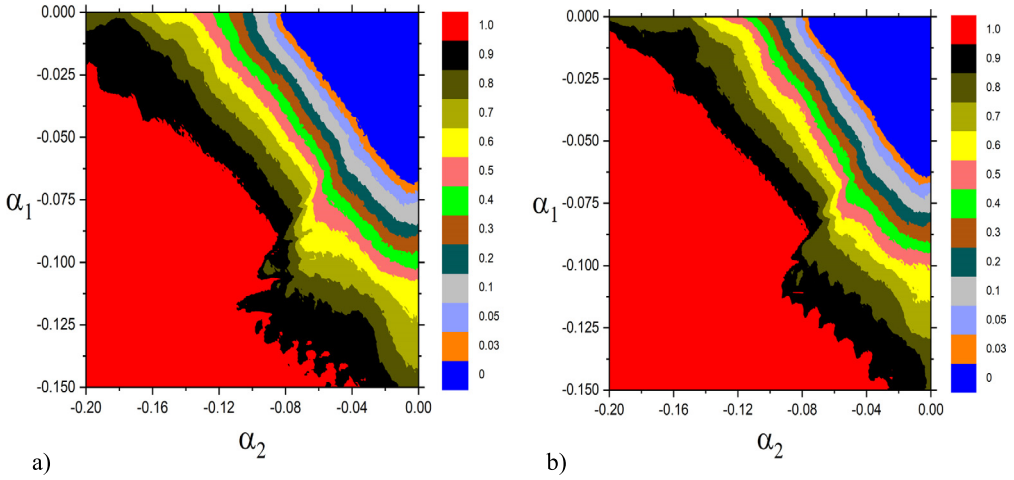


**Fig. 7.** Space of parameters depicted in a color scale representing the ratio of initial conditions that crossed the position of the transport barrier. The other colors represent the stickiness intensity. The blue color means that the barrier is still acting, while it does not exist for the red region. The initial conditions used were, $I_0 \in [0.75, 0.9]$, $\chi_0 \in [0, 1]$ and $\varphi_0 = 0.5$. a) case of 4 Volts bias; b) case of 8 Volts bias.

tio of trajectories that have crossed the region where there were transport barriers, for each pair of $\alpha_1$ and $\alpha_2$. The condition used to assess whether the trajectory from an initial condition crossed the barrier comes from the observation that the barriers are limited between $I \sim [0.25, 0.73]$ in the phase space. Therefore, for an initial condition given above $I_0 > 0.73$, if the trajectory reaches $I < 0.25$, or vice-versa, it follows that the trajectory crossed the barrier region.

The color scale in Figs. 7a and 7b represents the ratio of initial conditions that crossed the transport barrier region. The dark blue color represents parameters for which the barriers are identified. The other colors indicate the stickiness effectiveness. In particular, the red colors represent parameters for which no barriers are observed.

Both space parameters presented in Fig. 7a and Fig. 7b are qualitatively similar in the sense that only a small area representing less than 20% (dark blue region) indicates that these barriers exist. We can also see in Fig. 7a and Fig. 7b for high parameter values, in absolute values, more and more initial conditions are crossing the barriers as the red color dominates both parameter spaces. Therefore, the increase of the parameter values, in absolute values, leads to a decrease in the effectiveness of the barriers.

## 4. Conclusion

In this work, we introduced a new three-dimensional nonlinear map to describe shearless transport barriers in magnetically confined plasmas in a drift wave model with two dominant modes.

For the numerical applications, we considered plasma equilibrium profiles similar to those observed in Texas Helimak, modified by the bias, an external electric field, applied to control turbulence and transport. This modified electric field profiles are nonmonotonic and the resulting map violates the twist condition, giving rise to shearless transport barriers in phase space. Furthermore, by fixing the amplitude of the first mode and varying the amplitude of the second one, we investigate the existence of the shearless barriers and compute the critical parameter values for their destruction. Thus, examining the particle trajectories winding numbers and their recurrence, we show that the barriers existence previously predicted for one dominant drift mode are limited by the second mode amplitude increasing.

Despite the destruction of regular structures in the phase space, we also observed stickiness reducing the transport where the shearless curve was previously located. Then to evaluate the effectiveness of the transport barriers, for both biases, we analyzed the space of parameters, depicted in a color scale, which showed that as the wave amplitudes increase, the effectiveness of the barriers decrease. However, choosing appropriately the amplitudes of the waves it is possible to preserve the transport barriers (as showed in the blue regions of Fig. 7) and consequently to have a better confinement even with two modes acting in the plasma.

## CRediT authorship contribution statement

**L.F. Bernardi de Souza:** Writing – review & editing, Writing – original draft, Methodology, Investigation, Formal analysis, Data curation. **R. Egydio de Carvalho:** Writing – review & editing, Methodology, Investigation, Formal analysis, Conceptualization. **I.L. Caldas:** Writing – review & editing, Methodology, Investigation, Formal analysis, Conceptualization.

## Declaration of competing interest

The authors declare that they have no known competing financial interests or personal relationships that could have appeared to influence the work reported in this paper.

## Acknowledgements

REC and ILC acknowledge support from the Brazilian scientific agency FAPESP–São Paulo Research Foundation through Grants 2019/07329-4 and 2018/03211-6 respectively. ILC also thanks support from CNPq – National Council for Scientific and Technological Development, Grant 302665/2017-0.

## References

[1] R.D. Hazeltine, J.D. Meiss, Plasma Confinement, Dover Publications, Mineola, N.Y, 2003.
[2] C.W. Horton, Turbulent Transport in Magnetized Plasmas, World Scientific, 2012.
[3] G. Schmidt, Physics of high temperature plasmas, in: Physics of High Temperature Plasmas, 2nd ed., Academic, New York, 1979, p. 161.
[4] W. Horton, Hyoung-Bin Park, Jae-Min Kwon, D. Strozzi, P.J. Morrison, Duk-In Choi, Drift wave test particle transport in reversed shear profile, Phys. Plasmas 5 (1998) 3910.
[5] W. Horton, Jean C. Perez, K. Gentle, W.L. Rowan, K. Lee, Russel B. Dahlburg, Drift wave instability in the Helimak experiment, Phys. Plasmas 13 (2006) 032101.
[6] W. Horton, Drift waves and transport, Rev. Mod. Phys. 71 (1999) 735.
[7] R. Egydio De Carvalho, A.M. Ozorio De Almeida, Integrable approximation to the overlap of resonances, Phys. Lett. A 162 (1992) 457.

[8] J.D. Meiss, Sympletic maps, variational principles and transport, Rev. Mod. Phys. 64 (1992) 795.
[9] D. Del Castillo-Negrete, J.M. Greene, P.J. Morrison, Area preserving non-twist maps: periodics orbits and transition to chaos, Physica D 91 (1996) 1.
[10] J.D. Szezech, I.L. Caldas, S. Lopes, P.J. Morrison, R.L. Viana, Effective transport barriers in nontwist maps, Phys. Rev. E 86 (2012) 036206.
[11] C.G.L. Martins, R. Egydio de Carvalho, I.L. Caldas, M. Roberto, Labyrinthic standard non-twist map, J. Phys. A, Math. Theor. 44 (2011) 045102.
[12] R.M. Ferro, I.L. Caldas, Internal transport barriers in plasmas with reversed plasma flow, Phys. Lett. A 15 (2018) 382.
[13] K.W. Gentle, H. Huang, Texas Helimak, Plasma Sci. Technol. 10 (2008) 284.
[14] D.L. Toufen, F.A.C. Pereira, Z.O. Guimarães-Filho, I.L. Caldas, K.W. Gentle, Phys. Plasmas 29 (2022) 042303.
[15] K.W. Gentle, K. Liao, K. Lee, W.L. Rowan, Comparison of velocity shear with turbulence reduction driven by biasing in a simple cylindrical slab plasma, Plasma Sci. Technol. 12 (2010) 391.
[16] C. Hidalgo, On the nature of transport in fusion plasmas, Astrophys. Space Sci. 292 (2004) 681.
[17] D.L. Toufen, Z.O. Guimarães-Filho, I.L. Caldas, J.D. Szezech, S. Lopes, Analysis of the influence of external biasing on Texas Helimak turbulence, Phys. Plasmas 20 (2013) 022310.
[18] D.L. Toufen, Z.O. Guimarães-Filho, I.L. Caldas, F.A. Marcus, K.W. Gentle, Turbulence driven particle transport in Texas Helimak, Phys. Plasmas 19 (2012) 012307.
[19] D.L. Toufen, Controle de turbulência em plasmas, Ph.D. Thesis, Institute of Physics, University of São Paulo, 2012, https://www.teses.usp.br/teses/disponiveis/43/43134/tde-26032013-154737/publico/TOUFENDLtesedoutorado.pdf.
[20] N. Slater, Gaps and steps for the sequence n$\theta$ Mod 1, Math. Proc. Camb. Philos. Soc. 63 (1967) 1115.
[21] E.G. Altmann, G. Cristadoro, D. Pazó, Nontwist non-Hamiltonian systems, Phys. Rev. E 73 (2006) 056201.
[22] C.V. Abud, I.L. Caldas, On Slater's criterion for the breakup of invariant curves, Physica D 308 (2015) 34.
[23] L.A. Osorio, M. Roberto, I.L. Caldas, R.L. Viana, Y. Elskens, Onset of internal transport barriers in tokamaks, Phys. Plasmas 28 (2021) 082305.